Chapter 5

Magnetic Resonance (MR)-transverse relaxivity in ensembles of isotropic nanoparticles

5.1 INTRODUCTION

In the platform of smart imaging modality like Magnetic Resonance Imaging (MRI), engineered nanomagnets having tailored magnetic characteristics shows significant impact on enhancing faster water proton dephasing during relaxation decay [1-8]. However, in comparison to primary nanomagnet, an ensemble of magnetic nanoparticles [9-15] is an intriguing approach to pursue efficient transverse-relaxivity (r_2) [8, 12]. Traditionally, classical Soloman-Bloembergen-Morgan (SBM) theory explains the correlation of longitudinal-transverse relaxivity of water protons with dipole-dipole interactions considering both proton-proton interaction and proton-electron interaction [16, 17, 18]. In quantum-mechanical outer-sphere theory, MR-relaxivity of ensembles depends on shape/size, composition, water penetration property, etc. But, for superparamagnetic NPs, quantum-mechanical outer-sphere theory can explain the transverse relaxivity only up to a critical size, which can satisfy the outer-sphere motional averaging regime (MAR) condition [24, 25]. MAR explains that transverse relaxivity is dependent on water proton diffusion and inherent physical characteristics of MNPs, which can be modulated by tuning structural properties, crystal structure, and surface-induced behaviours along with dephasing of protons in single domain MNPs [26, 27, 28, 29. 30, 31].

In a cluster of multi-domain nanoparticles, the process of proton dephasing is complicated to explain. Indeed, static dephasing regime (SDR) [32] and echo-limiting regime [33] have to be considered to explain the transverse relaxivity,

when nanoparticles' size exceeds the ideal MAR threshold limit, which results in complications in explaining the r_2 relaxivity. Additionally, adjacent nanoparticles in ensembles can engender a higher degree of complexity in the local field because of the reduction of magnetic local field symmetry. Hence higher degree of field inhomogeneity induces perturbation to proton phase coherence due to the diffusion of water molecules around MNPs which can modulate transverse relaxivity [34, 35, 36]. The specific arrangement of atoms, crystal structures, moment alignment, and long-range/short-range order of spins can trigger crystalline anisotropy of MNPs leading to transverse relaxivity modulation. Moreover, although the correlation between saturation magnetization and transverse relaxation is validated for single-domain MNPs in MAR which is based on net proton dephasing, there is an ambiguity for multi-domain clusters of MNPs to establish coordination among magnetic saturation, proton dephasing, and r_2 relaxivity [36, 37, 38].

In this chapter, the underneath mechanism of transverse MR-relaxivity is explained following magnetic anisotropy in ensembles of isotropic nanoparticles, $Ni_{1-x}Zn_xFe_2O_4$@CoO (x=0.25, 0.50). The core-shell architecture is essential for the relaxation mechanism since the electrical configuration of the shell of magnetic nanoparticles (CoO) differs from the core ($Ni_{1-x}Zn_xFe_2O_4$). The spin canting, as well as the easy axes organization of CoO with non-magnetic Zinc ions substitution in octahedral site of core in $Ni_{1-x}Zn_xFe_2O_4$@CoO (x=0.25, 0.50), are crucial parameters to explore MR-relaxation mechanism. The exchange field-induced inhomogeneous anisotropy induced in such complex structures triggers the faster transverse relaxation. The magneto-crystalline anisotropy landscape is executed by considering thermal energy-dependent anisotropy constant and competition among moments. The modulation in easy axes alignment is justified by varying the crystal dopants/lattice substitution. A relation of anisotropy energy with magnetic moment alignment as well as interaction competition of moments is drawn with the enhancement in transverse MR-relaxivity. The

coupling among the nanoparticles in an assembly structure with reduced magnetization can modulate the transverse relaxation. The ground state magnetization is executed with DFT simulation. The 25% Zn ion substitution in $NiFe_2O_4$ octahedral site in $Ni_{1-x}Zn_xFe_2O_4$@CoO shows enhanced cell-viability for HEK cell-line, potential cytotoxicity against MCF-7 breast cancer cell-line, and the systems show no pro-tumorigenic activity.

5.2 EXPERIMENTAL DETAILS

5.2.1 Synthesis technique

The synthesis is followed by co-precipitation technique [39] with a two-step synthesis procedure. $Zn(NO_3)_2.6H_2O$ is used as a Zinc precursor, $Co(NO_3)_2.6H_2O$ is used as a Cobalt precursor, $Ni(NO_3)_2.6H_2O$ is used as a Nickel precursor, and $FeCl_3.6H_2O$ is used as Fe precursor, and sodium hydroxide (NaOH) solution is considered. The formation of Zn substituted Nickel Ferrite is followed as a stoichiometric Zinc Nitrate hexahydrate amount is mixed with nickel nitrate hexahydrate as well as ferric chloride hexahydrate in a deionized water of 100mL. The solution is maintained at 10 pH following NaOH addition. The achieved brown-coloured solution is kept for stirring for a period of 3 h at 80°C. Once the digestion is completed, the precipitate is separated by the application of a magnet followed by washing with alcohol. The blackish powder is kept to get dried for 12 h. The achieved powdered sample is considered for calcination at 400°C for 6 hrs. After cooling, obtained black powder is kept. Two varied stoichiometric Zinc Nitrate hexahydrate amounts are considered with nickel-nitrate-hexahydrate and ferric-chloride-hexahydrate for $Ni_{0.75}Zn_{0.25}Fe_2O_4$ and $Ni_{0.5}Zn_{0.5}Fe_2O_4$. During the second part of synthesis, 1 mM of cobalt-nitrate-hexahydrate amount is kept in deionized water in 100 mL with a Zn substituted system dispersed during stirring and kept for sonication for ½ hr. Later, a solution of NaOH is mixed dropwise to get 10 pH. The precipitation is achieved. The obtained precipitate is separated from solvent and washed by alcohol. Once

the system is dried, black powder is considered for 200°C calcination for 3h. A CoO layer is decorated over $Ni_{1-x}Zn_xFe_2O_4$ MNPs, giving $Ni_{1-x}Zn_xFe_2O_4$@CoO. With Zn concentration variation, $Ni_{0.75}Zn_{0.25}Fe_2O_4$@CoO is addressed for 25% Zn substitution and $Ni_{0.50}Zn_{0.50}Fe_2O_4$@CoO is addressed for 50% Zn substitution in Ni-site. The rest of the instrument information is similar to the previous chapter. In addition, Zeta Potential analysis is executed in NanoPlus-3, Nano Particle Analyzer.

5.2.2 Magnetic Resonance Imaging (MRI) analysis

Magnetic Resonance (MR)-relaxivity is executed at Siemens skyra Magnetom MRI instrument of 3 T.

5.2.3 Cytotoxicity

Human Embryonic kidney (HEK-293) cell lines which are non-cancerous in nature and Michigan Cancer Foundation cell lines MCF-7, cancerous in nature were used to perform MTT (3-(4,5-Dimethylthiazol-2-yl)-2,5-Diphenyltetrazolium Bromide) assay. As the kidney plays an important role in filtration of metabolic wastes and fluids and MNPs have a propensity for renal clearance and its functionality, their exposure to the kidney might affect its function. As such, cellular toxicity assessment is a necessity for these synthesized systems. HEK-293 and MCF-7 cell lines were maintained in DMEM medium supplemented with 10% of FBS and Pen-Strep. This was allowed to incubate at 37°C. In a 96-well plate,10^4 cells were seeded per well followed by MNPs treatment for 24 h period with the concentration of MNPs ranging up to 1mM. Post-treatment, 15 µl MTT (5 mg/ml) concentration was added and incubated again for 3 h. The formazan crystals formed after MTT addition were dissolved and the absorbance of the same was taken at 590 nm using a MultiSkan^{TM}GO spectrophotometer (Thermo Fisher Scientific, USA). Olympus model fluorescence microscope (IX83 Japan) was used to obtain the cell images pre-and post-treatment.

5.3 COMPUTATIONAL DETAILS

For ground state magnetization analysis, first-principle-based DFT calculations are executed for two different substitutions of Zinc on a nickel site in nickel ferrite, considering 25% and 50% substitution. The systems are addressed as, $Ni_{0.75}Zn_{0.25}Fe_2O_4$, $Ni_{0.5}Zn_{0.5}Fe_2O_4$ as depicted in Figure 5.1(c) and(d). The core-shell structure of $Ni_{0.75}Zn_{0.25}Fe_2O_4$@CoO and $Ni_{0.5}Zn_{0.5}Fe_2O_4$@CoO is given in Figure 5.1(g) and (h) respectively. The spin-polarization effect is employed to retain the ferromagnetic order in the system. The atomic configurations optimization and respective calculation of electronic structure are executed by using the QUANTUM Espresso (QE) [49, 50] software package. In the two different sets, 56 atoms are considered for the doped system in a single unit cell and 198 atoms for core-shell systems in their unit cell to perform DFT. Broyden-Fletcher-Goldfarb-Shanno (BFGS) algorithms are used in optimized configuration. The substitution of 25% Zn in the unit cell comprises 532 electrons with 319 Kohn-Sham (KS) states. 496 electrons and 298 KS states are present in the 50% Zn-substituted system. The respective unit cell of core-shell structure contains 1776 electrons with 1066 KS states for 25% substitution and 1780 electrons with 1068 KS states for 50% substitution. The USPP developed through a method named RRKJ for electron-core connections. The outer shell of Co is organised with nine valence electrons ($4s^2\ 3d^7$) as well and Nickel [Ni(O_h)] atoms are arranged with ten valence electrons ($4s^2\ 3d^8$). The substitution of Zn in the octahedral site replaces the nickel [Zn(O_h)] having two valence electrons ($4s^2\ 3d^{10}$). The Iron [Fe(O_h) and Fe(T_d)] comprises valence electrons of number 8 ($4s^2\ 3d^6$) with 6 valence valence electrons of oxygen (O) ($2s^2\ 2P^4$). The terms T_d and O_h address tetrahedral and octahedral sites. The self-consistent local density approximation (LDA) is considered for exchange-correlation function as per Perdew and Wang (PW). The considered BZ sampling is 3 x 3 x 3 Monkhorst-pack having an unshifted *k*-mesh grid. For a core-shell system with 198 atoms, the *k*-mesh grid is taken as 1 x 1 x 1 for computational cost as well as time

reduction to get the convergence. 50 Ry of cut-off energy is taken having 10^{-6} Ry convergence threshold, and afterwards Davidson diagonalization. In addition, a denser k-mesh grid having 12 x 12 x 12 is considered through the tetrahedron method having Bloch modifications to get more accuracy in electronic structure calculation. For density of states (DOS) calculation, a 2 x 2 x 2 k-mesh grid is considered with the tetrahedron method.

5.4 RESULTS AND DISCUSSIONS

5.4.1 Microstructural analysis

The FESEM and TEM micrographs confirmed the development of core-shell MNPs with a size variation of 8-10 nm and a cluster of sized 100 nm-120 nm is confirmed as depicted in Figure 5.1 (a, b, e, f). However, Figure 5.1(c) provides optimized crystal geometry having 25% Zn substitution in nickel ferrite, addressed as $Ni_{0.75}Zn_{0.25}Fe_2O_4$. In Figure 5.1(g), another crystal geometry of 50% Zinc substituted nickel ferrite is considered, $Ni_{0.5}Zn_{0.5}Fe_2O_4$. In a unit cell, 56 atoms are considered in 25% Zn-substituted systems with 16 Fe atoms, 6 Ni atoms with 2 number of Zn atoms. In a 50% Zn-substituted system, 8 atoms of Fe, Ni, and Zn are considered [40, 41]. In both cases, the perennial 32 oxygen atom bonds with divalent Ni^{2+} cation, which is further substituted with the aid of Zn^{2+} cation and Fe^{3+} trivalent cations with O^{2-} ions to achieve a face-cantered cubic (FCC) lattice. The lattice parameter of respective $Ni_{0.75}Zn_{0.25}Fe_2O_4$ and $Ni_{0.5}Zn_{0.5}Fe_2O_4$ is achieved as 8.48 Å and 8.36 Å. The magnetization is achieved as 38.9 and 29.8 μ_B/cell for $Ni_{0.75}Zn_{0.25}Fe_2O_4$ and $Ni_{0.5}Zn_{0.5}Fe_2O_4$ following a self-consistent approach. With enhanced Zn substitution, Curie temperature, T_C, the reduction is expected. However, T_C is found to be lowered when the core is combined with a shell of cobalt oxide (CoO) layer in order to achieve a core-shell structure.

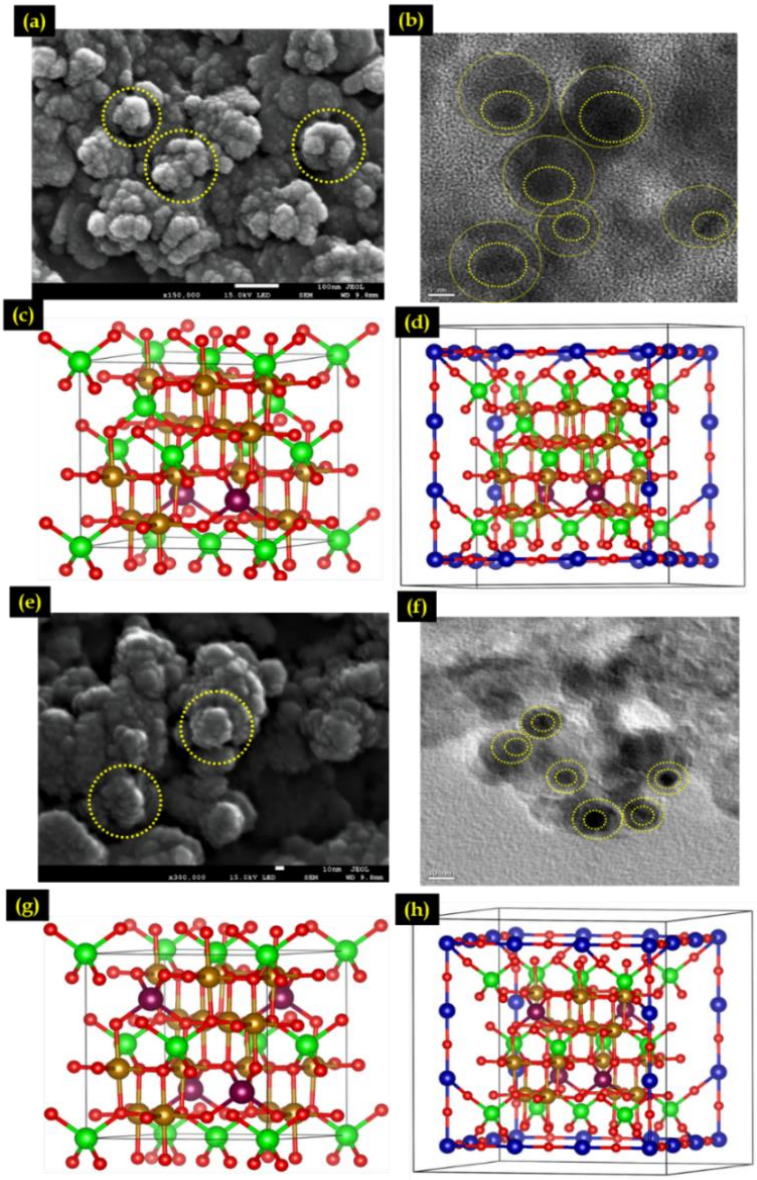

Figure 5.1: (a) FESEM micrographs of system 1 in scale bar of 100 nm, (b) TEM micrographs of system 1 in the range of 5 nm; The stable crystal geometry (c) $Ni_{0.75}Zn_{0.25}Fe_2O_4$, (d) $Ni_{0.75}Zn_{0.25}Fe_2O_4$@CoO, (e) FESEM micrograph of system 2 in the range of 10 nm, (f) TEM micrograph of system 2 in the range of 10 nm; stable crystal geometry of (g) $Ni_{0.5}Zn_{0.5}Fe_2O_4$, (h) $Ni_{0.5}Zn_{0.5}Fe_2O_4$@CoO. For Co, Zn, Ni, Fe, and O, the colours blue, violet, green, golden and red are given.

However, in Figure 5.1(d) and Figure 5.1(h), optimized atomic configuration for both $Ni_{0.75}Zn_{0.25}Fe_2O_4$@CoO and $Ni_{0.5}Zn_{0.5}Fe_2O_4$@CoO is depicted. For cobalt atoms, a blue colour is given; for nickel, a green colour is given, for zinc, a violet

colour is given, for iron, golden colour is given, and for oxygen, red colour balls are given. For a single unit cell, 198 atoms are considered with 16.08 Å lattice parameter, for both cases. The magnetization value is achieved as 210.67 and 207.16 μ_B/cell for $Ni_{0.75}Zn_{0.25}Fe_2O_4$@CoO and $Ni_{0.5}Zn_{0.5}Fe_2O_4$@CoO. With Zn-substituted core as well as core-shell systems, total magnetization is found to be decreased in both systems.

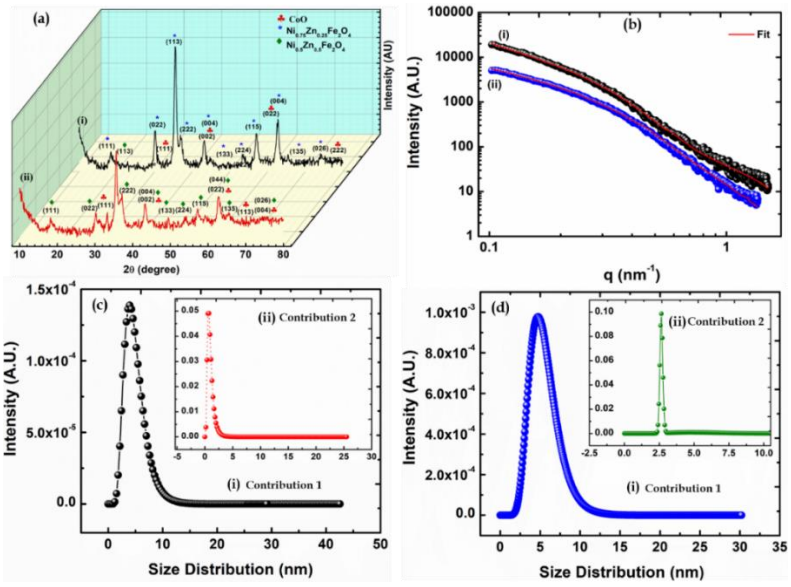

Figure 5.2: (a) XRD plot for (i) system 1, (ii) system 2; (b) SAXS intensity profile fitting for (i) system 1, (ii) system 2: (c) Size distribution plot for system 1, and (d) Size distribution plot for system 2.

In order to confirm the crystallographic phase, Figure 5.2(a) depicts XRD plots for both systems. Figure 5.2(a(i)) shows the prominent peaks for (111), (002), (022), and (222) planes supporting the formation of cubic Cobalt Oxide (CoO) phase as validated from HighScore Plus reference: 98-005-3057. In addition, the observed planes, such as (111), (022), (113), (222), (004), (133), (224), (115), (004), (135), and (026) confirm the $Ni_{0.75}Zn_{0.25}Fe_2O_4$ phase, validated from reference code of 98-016-3785. Therefore, $Ni_{0.75}Zn_{0.25}Fe_2O_4$@CoO phase is ensured for System 1 [42, 43]. As displayed in Figure 5.2(a(ii)), the respective planes of (111), (002), (022), (113), and (222) confirm the CoO cubic phase. Along with these

planes, additional planes are found in, (113), (022), (111), (222), (004), (133), (224), (115), (044), (135), (026), and (444) ensuring the development of $Ni_{0.5}Zn_{0.5}Fe_2O_4$ as validated from HighScore plus with reference number 98-009-6663. Therefore, System 2 can be addressed as $CoO@Ni_{0.5}Zn_{0.5}Fe_2O_4$ [42, 43].

In Figure 5.2(b), the SAXS intensity profile is displayed with a double logarithmic scale. The morphology of core-shell structure is evident from the scattering analysis. However, the contribution 1 is believed to originate from MNPs, and the contribution 2 is considered to arise from the interparticle distance between nanoparticles. Together, these two components are observed as cumulative scattering resulting in net scattering intensity profile. The log-normal distribution function is followed by the intensity profile fitting as,

$$logNorm(x) = N\, x^{-p} \exp\left[-(ln(x) - \ln(\mu))^2 / 2s^2\right] \quad (5.1)$$

with $$\int_0^\infty logNorm(x) = N \quad (5.2)$$

Here, the letter "s" designates the poly-dispersity index with nanoparticle radius "μ" in nanometers. In contribution 1, it is assumed that the spherical shell form factor, $F(q, R_1, R_2, \mu, \eta)$, fits log-log plot for the systems having R (radius). Herein, R_1 is the outer shell radius and R_2 is the radius of inner core), following the equation:

$$F(q, R_1, R_2, \mu, \eta) = K(q, R_1, \eta) - K(q, R_2, \eta(1-\mu)) \quad (5.3)$$

with $$K(q, R, \eta) = \frac{4}{3}\pi R^3\, \eta\, 3[\sin(qR) - qR\cos(qR)] / (qR)^3 \quad (5.4)$$

Here, η gives scattering contrast for the shell with μ as inner core scattering contrast. The spherical form factor is regarded, P(q, R), following the equation:

$$P(q, R) = 9\,[\sin(qR) - qR\cos(qR)]^2/(qR)^6] \quad (5.5)$$

However, mass fractal having expected cut-off function h(r, ξ) is taken in the contribution 1 as:

$$I(q) = \int N(R)F^2(q,R)S(q,R)dR \tag{5.6}$$

In which, S(q, R) gives a structure factor along with cut-off length of ξ. The monomer radius is addressed as χ, with fractal dimension noted as D and the corresponding structure factor S (q, R) is written as:

$$S(q,R) = 1 + \frac{D}{\chi^D}\int_0^\infty R^{D-3}h(\mathrm{r},\xi)\frac{\sin(qr)}{(qr)}r^2dr \tag{5.7}$$

The mass fractal structure factor with the dimension of 1.8 is achieved for system 1 and a dimension of 3 is found for system 2 for contribution 1. While considering contribution 2, there is the absence of structure factor in both the systems. The achieved parameters from fittings are provided in Table 5.1 and Table 5.2. However, distribution plots of MNPs size are depicted in Figure 5.2(c) and Figure 5.2(d).

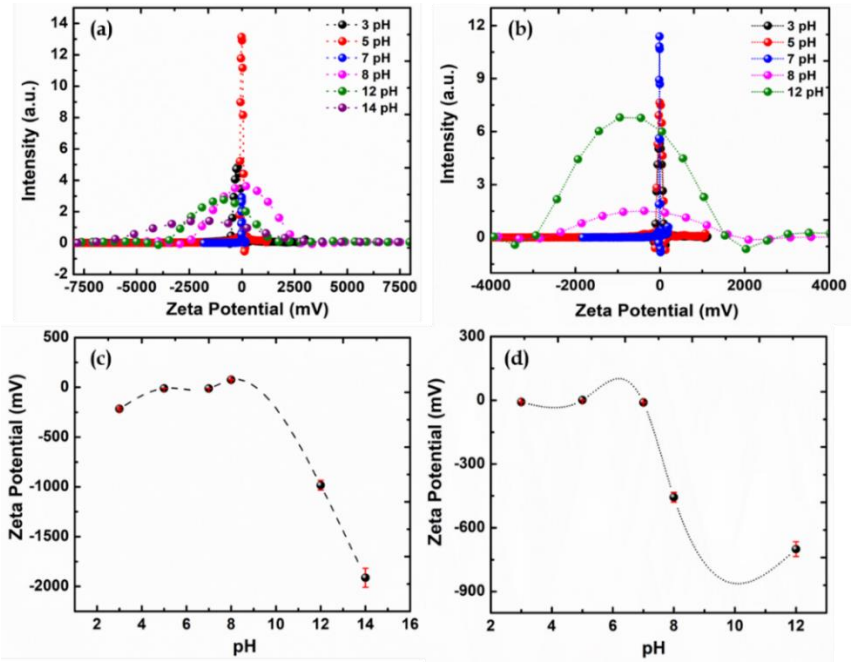

Figure 5.3: (a) Zeta potential plots for system 1, (b) Zeta potential plots for system 2, pH variation trend with Zeta potential (c) system 1, $Ni_{0.75}Zn_{0.25}Fe_2O_4$@CoO, and (d) system 2, $Ni_{0.5}Zn_{0.5}Fe_2O_4$@CoO. The error bars in the data is standard deviation in experimental data.

Table 5.1. Fitting parameters for primary MNPs from SAXS intensity profile.

System	Contribution 1							
Name	Shape	Net size in nm (μ)	s	R_1	R_2	Structure factor		
						Type	χ_i	D
$Ni_{0.75}Zn_{0.25}Fe_2O_4$@CoO	Core-shell	4.950	0.440	2.950	2	Mass fractal	100.0	1.80
$Ni_{0.5}Zn_{0.5}Fe_2O_4$@CoO	Core-shell	5.30	0.350	20	3	Mass fractal	100.0	3.0

Table 5.2. Fitting parameters for primary MNPs from SAXS intensity profile.

Contribution 2			
System	Shape	s	R in nm
$Ni_{0.75}Zn_{0.25}Fe_2O_4$@CoO	Sphere	0.60	1.20
$Ni_{0.5}Zn_{0.5}Fe_2O_4$@CoO	Sphere	0.320	1.50

Indeed, surface charge on MNPs is accessed by considering zeta potential studies to forecast the stability and infer the state of the surface. as given in Figure 5.3(a, b) [12]. With variation in pH, the Zeta potential values are found as -216.30 mV at pH 3 for system 1, -9.70 mV at pH 5 for system 1, -11.10 mV at pH 7 for system 1, 76.60 mV at pH 8 for system 1, -983.90 mV at pH 12 for system 1, and -1912.50 mV at pH 14 for system 1; -8.0 mV at pH 3 for system 2, 1.20 mV at pH 5 for system 2, -10.30 mV at pH 7 for system 2, -456.10 mV at pH 8 for system 2, and -

700.50 mV at pH 12 for system 2, and the trend in pH is given in Figure 5.3(c) and Figure 5.3 (d).

In Figure 5.4, XPS is represented to get information regarding electronic states as well as compositions. The cobalt (Co) 2P spectra show two major peaks of Co $2P_{1/2}$ as well as Co $2P_{3/2}$ at 795.50 eV and 780.30 eV as depicted in Figure 5.4(a) $Ni_{0.75}Zn_{0.25}Fe_2O_4$@CoO. Two additional satellite peaks are evident at 786.50 eV and 804.80 eV for Co^{2+} ions. As depicted in Figure 5.4(f), at 795.30 eV and 780.0 eV the respective Co $2P_{1/2}$ and Co $2P_{3/2}$ peaks are observed with satellite peaks at 786.70 eV and 803.10 eV for $Ni_{0.5}Zn_{0.5}Fe_2O_4$@CoO. The observed energy difference of Co $2P_{1/2}$ and Co $2P_{3/2}$ is 15.20 eV for system 1 and 15.30 eV for system 2, supporting reporting values for CoO respectively [44]. For the Ni 2P spectrum, Ni $2P_{3/2}$ and Ni $2P_{1/2}$ peaks are found at 855.0 eV and 872.60 eV as depicted in Figure 5.4(b) for for system 1, and for system 2, 2P spectrum are found at 854.80 eV and 871.90 eV as depicted in Figure 5.4(g). The $2P_{3/2}$ and $2P_{1/2}$ peak difference of nickel is achieved as 17.60 eV and 17.10 eV for system 1 and system 2 respectively. The satellite peaks are found at around 861.6 eV and 879.6 eV for system 1 and 859.90 eV, 862.50 eV, 879.10 eV, and 882.40 eV for system 2 for Ni^{2+} state [45, 46]. The respective Zn $2P_{3/2}$ and Zn $2P_{1/2}$ peaks are found at 1021.80 eV and 1045.10 eV for system 1; and, 1021.0 eV and 1044.0 eV for system 2 as given in Figure 5.4(c) and Figure 5.4(h) [47, 48]. For Fe $2P_{3/2}$ and Fe $2P_{1/2}$, peaks are found at 711.30 eV and 723.70 eV for system 1 and 711.40 eV and 723.80 eV for system 2 as displayed in Figure 5.4(d) and 5.4(i). The satellite peaks are achieved at 710.0 eV, 713.30 eV, 715.0 eV, and 719.50 eV for system 1, and at 719.50 eV and 715.0 eV for system 2 [40]. The oxygen 1S is displayed in Figure 5.4(e) and Figure 5.4(j), with O 1S peak at 529.50 eV, 530.30 eV, 531.40 eV, 532.50 eV for system 1 and at 529.50 eV, 530.0 eV, 531.40 eV, and 532.50 eV for system 2. The metal oxide bonds are represented by O 1S spectrums [45, 46, 47, 48].

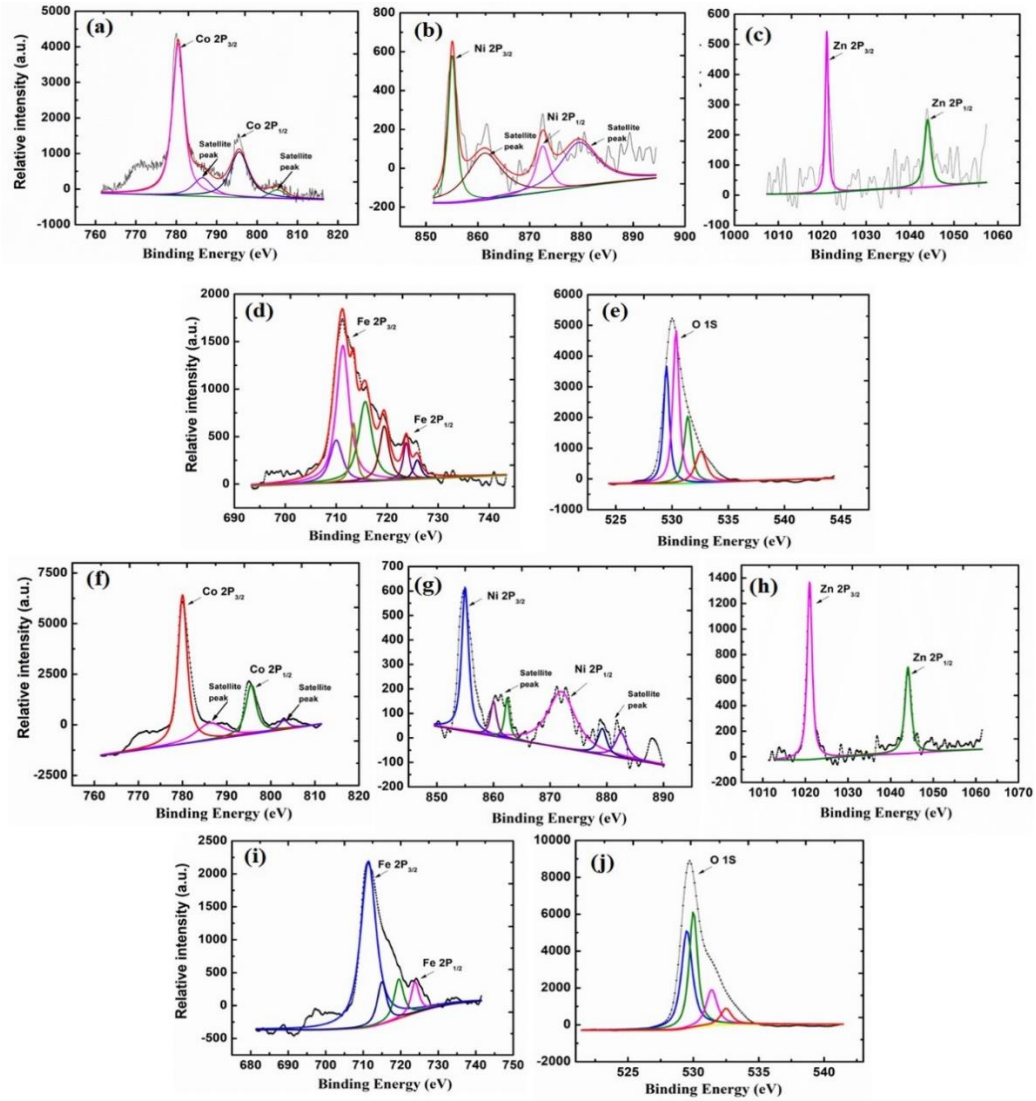

Figure 5.4: XPS for $Ni_{0.75}Zn_{0.25}Fe_2O_4$@CoO for (a) Co-2P spectrum, (b) Ni-2P spectrum, (c) Zn-2P spectrum, (d) Fe-2P spectrum, and (e) O-1S spectrum; For $Ni_{0.5}Zn_{0.5}Fe_2O_4$@CoO for (f) Co-2P spectrum, (g) Ni-2P spectrum, (h) Zn-2P spectrum, (i) Fe-2P spectrum, and (j) O 1S spectrum.

5.4.2 Atomic Configuration and Electronic Structure

In Figure 5.5, the electronic band structure along DOS is depicted. In Figure 5.5(a) and (b), the electronic band structure and DOS for $Ni_{0.5}Zn_{0.5}Fe_2O_4$ is addressed. The half-metallic behaviour is evident from the pronounced gap in up-spin channel as well as in the down-spin channel, overlapping states are reflected. From Figure 5.5(b), the DOS pattern at Fermi level further confirms half-

metallicity. The respective DOS pattern displays existence of an asymmetric spike-like nature, that ensures magnetic nature [40, 41].

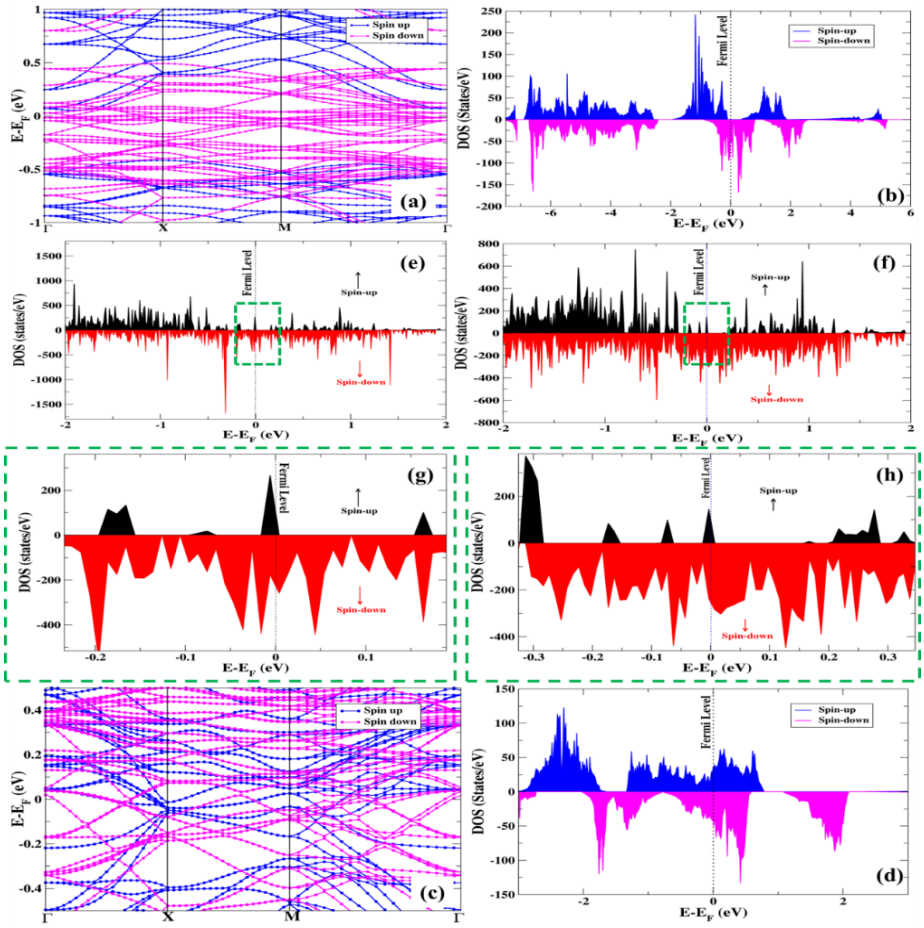

Figure 5.5: Electronic band structure as well as DOS calculation for (a, b) $Ni_{0.5}Zn_{0.5}Fe_2O_4$, (c, d) $Ni_{0.75}Zn_{0.25}Fe_2O_4$. Spin-dependent DOS for: (e) $Ni_{0.5}Zn_{0.5}Fe_2O_4$@CoO, (f) $Ni_{0.75}Zn_{0.25}Fe_2O_4$@CoO. The given green dashed box is magnified. (g) and (h) depicts the magnified image of core-shell systems.

The considered O atoms give a positive magnetic moment with +0.11 μ_B/cell, trivial average local moment. The respective magnetization of Ni atoms gives moment of -0.4698 μ_B/cell on average. For Fe in O_h and T_d, an average magnetization of +3.2 μ_B/cell is found. For Zn atoms, the magnetization of +0.042 μ_B/cell is found in Figure 5.5(b), the symmetric up and down-spin channel is evident from -7 to -2 eV stating the existence of Zn. The signature of Ni atom is confirmed at the Fermi level region of -1.5-1.5 eV and (-2)-(-1.5) eV. For 0.5 to 2.5

eV energy region, Fe atoms' existence is confirmed in the conduction band. From Figure 5.5(c) and (d), electronic band structure as well as DOS pattern confirm metallic nature in $Ni_{0.75}Zn_{0.25}Fe_2O_4$. At the Fermi level, band crossover with overlapping states is readily visible. As shown in Figure 5.5(a) and (b), half-metallic nature is observed in 50% Zn substitution and metallic emerges at 25% substitution as seen in Figure 5.5(c) and (d). In DOS pattern as depicted in Figure 5.5(d), asymmetric nature of both spin channels is visible. The average local moment for asymmetric magnetic moment trend (positive and negative) in O atoms is determined to be +0.024 B/cell. The net negative magnetic moment of Ni (O_h) atoms of -1.057 μ_B/cell is maintained.

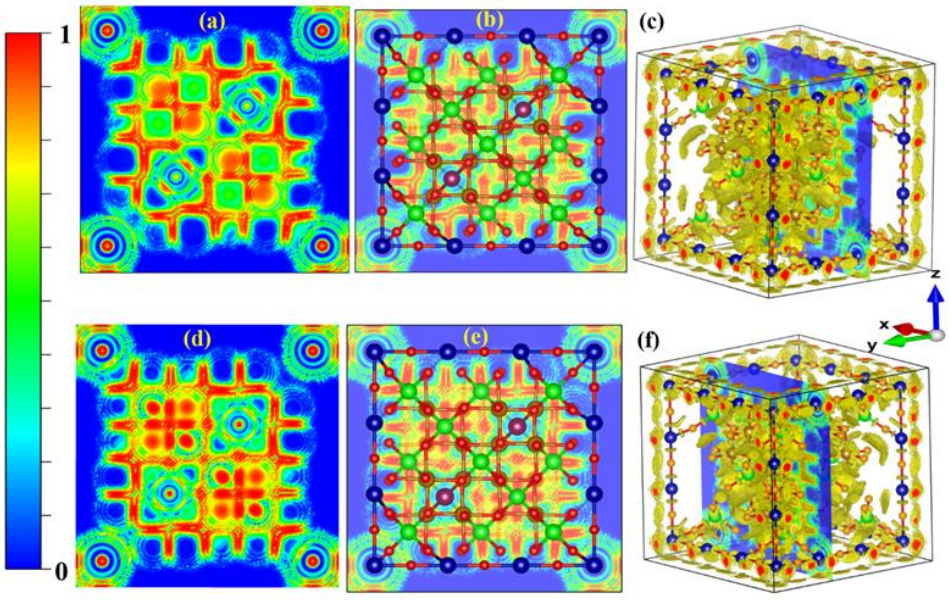

Figure 5.6: Density overlap region indicator (DORI) for (a-c) $Ni_{0.5}Zn_{0.5}Fe_2O_4$@CoO: 2D plot and 3D plots at (010) plane, (d-f) $Ni_{0.75}Zn_{0.25}Fe_2O_4$@CoO: 2D and 3D plot at (010) plane.

For Fe (O_h and T_d), the average moment is achieved as +2.57 μ_B/cell. The tiny local moment is seen to be induced in Zn atoms having a value of +0.0191 μ_B/cell. The Zn substitution at the Ni (O_h) site can impact d-orbital localization of Fe (T_d) site. Additionally, Zn-substitution at Ni (O_h) is relatively insensitive for Fe (T_d) site. Ni (O_h) sites are predominance in both up and down spin channels in valence

band below the Fermi level. Fe (O_h and T_d) sites at the fermi level are more susceptible to spin up and down channels due to higher O (p-orbitals) hybridization than Ni (O_h) sites due to lower Zn-substitution concentration.

In Figure 5.5(e) and Figure 5.5(f), spin-polarized DOS of $Ni_{0.5}Zn_{0.5}Fe_2O_4$@CoO and $Ni_{0.75}Zn_{0.25}Fe_2O_4$@CoO are given and the magnified images are depicted in Figure 5.5(g) and Figure 5.5(h). From DOS pattern, metallic nature of core-shell systems is evident having overlapping states at the Fermi level as displayed in Figure 5.5(g) and (h). However, Figure 5.5(g) ensures that 50% Zn-substituted core-shell structure has +1.810 μ_B/cell magnetization of Co, +0.949 μ_B/cell for Ni (O_h), +1.705 μ_B/cell for Fe (O_h and T_d), +0.46 μ_B/cell of O, and +0.0531 μ_B/cell for Zn. Figure 5.5 (h), 25% Zn-substituted core-shell structure shows +1.810 μ_B/cell magnetization of 32 Co atoms and asymmetric magnetization value having +0.99 μ_B/cell is evident for 16 Ni (O_h) atoms. The achieved magnetization for 16 Fe (O_h and T_d) atoms is found as +1.55 μ_B/cell. In 132 O atoms, a moment of +0.46 μ_B/cell is achieved. In Zn surrounded by Fe and O, trivial moment of +0.0527 μ_B/cell is found. From Figure 5.5(g) and (h), achieved spin-up and spin-down channels confirm existence of CoO and $Ni_{1-x}Zn_xFe_2O_4$. As depicted in Figure 5.5(g) and Figure 5.5(h), spin-up channel overlapping is seen near Fermi level because of weak hybridization between d-orbital of Co and p-orbital of O. From DOS patterns as given in Figure 5.5(g) and (h), up-spin channel as well as down-spin channel are seen as following asymmetric nature exhibiting non-zero net magnetic moment.

In Figure 5.6, the electron density overlap region for (010) plane is depicted. The 2D mapping of DORI is represented in Figure 5.6(a) and (b) for $Ni_{0.5}Zn_{0.5}Fe_2O_4$@CoO considering (010) plane. For the 3D plot, an isosurface value of 0.93 e/Å^3 is considered i to visualize the associated charges of the atoms. DORI values range from 0 to 1 as seen in the colour bar to represent the intensity of overlap region of electron density. From Figure 5.6(a) and (b), the contribution of electron density is given with 0-1 intensity range. The density of electrons near

Zn is comparatively low due to non-magnetic Zn. The existence of imposed magnetic nature from neighbouring Fe atoms is shown by slightly greater electron density that is seen in the red hue around an adjacent Zn atom. The van der Waals (vdW) type of interatomic interaction is ascribed, as represented in green colour. The density of electrons around the Ni atom and its neighbouring Fe atom shows enhanced electron density as depicted in red colour, which is due to strong interatomic interaction in inherent magnetic characteristics. In corner Co atoms, the evidence of electron localization (as marked in red colour) and delocalization (as marked in green colour) is confirmed with electronic charge in the surroundings as marked in red colour. The respective charges of each atom are depicted in 3D mapping form for density overlap region as given in Figure 5.6(c). In Figure 5.6(d-f), electron density overlap region is given in $Ni_{0.75}Zn_{0.25}Fe_2O_4$@CoO for the plane (010). The Zn-substituted region has a little greater core electron density because its adjacent atoms get fewer unpaired electrons, which causes a minor reduction in the magnetic moment [47, 48]. Due to its magnetic behaviour, the larger electron density is seen close to the Ni and Fe sites, which suggests a strong robust interaction as well as repulsion between two nearby atoms. The Zn substitution causes an alteration in the gradient of electron density overlap. The density overlap is present in Co atoms of core-shell structures, which is well supported by the observed magnetic moment. A higher electron density is found in system 1 compared to system 2, but a reduction of the moment in the Zn atom is achieved. As observed in Figure 5.6 of both the upper as well as lower panels, the substitution can modulate electron density following the interaction of neighbouring atoms in the region of substitution and bonding among nearby atoms. In both systems, an asymmetric electron distribution is exhibited outside the substituted region. With a variation of octahedral site substitution, the modulation in inherent properties is anticipated. Therefore, the in-detail magnetic study is performed experimentally.

5.4.3 Direct Current Magnetization Study

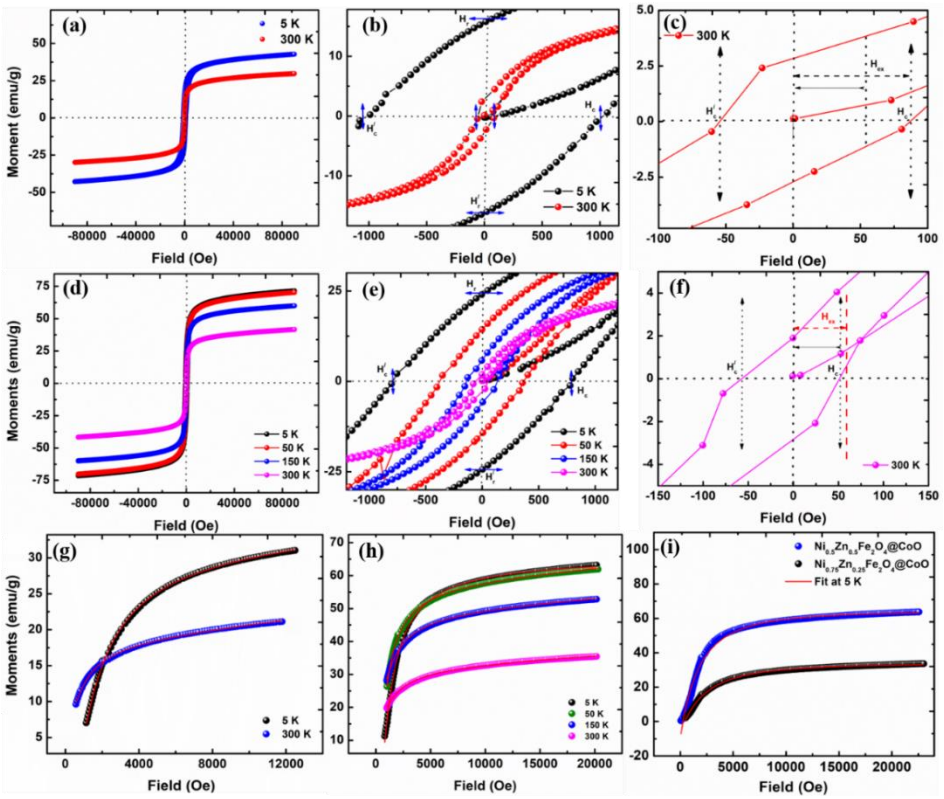

Figure 5.7: Field relying magnetization for (a) $Ni_{0.75}Zn_{0.25}Fe_2O_4$@CoO, (d) $Ni_{0.5}Zn_{0.5}Fe_2O_4$@CoO, Zoomed field relying magnetization for (b) $Ni_{0.75}Zn_{0.25}Fe_2O_4$@CoO, (e) $Ni_{0.5}Zn_{0.5}Fe_2O_4$@CoO, Asymmetric coercive field for (c) $Ni_{0.75}Zn_{0.25}Fe_2O_4$@CoO, (f) $Ni_{0.75}Zn_{0.25}Fe_2O_4$@CoO, LAS fitting for (g) system 1, and (h) for system 2, (i) RAT fit.

In Figure 5.7, field-relying magnetization is performed at 5 K as well as 300 K. Coercivity, H_c is calculated as, 1033.50 Oe at 5 K, 70.50 Oe at 300 K and 792.50 Oe at 5 K and 53.70 Oe at 300 K for system 1 and system 2. In system 1, remanence, H_r, is found as 2.740 emu/g at 300 K and 16 emu/g at 5 K; for system 2, H_r is 2.30 emu/g at 300 K and 24.0 emu/g at 5 K. With the increase in Zn substitution, a decrease in coercivity is achieved. Moreover, an asymmetric coercive-return magnetization trend is evident at 300 K [51, 52] as depicted in Figure 5.7(c), (f). This is due to unidirectional anisotropy energy observed in exchange coupling-dominated systems. The asymmetry field is achieved as 30.0 Oe and 5.0 Oe for

system 1 and system 2 at 300 K. Further, magneto-crystalline anisotropy constant is achieved using LAS fitting. LAS model fitting is performed using equation 2.7 of Chapter 2 and represented in Figure 5.7 (g, h) for both 300 K and 5 K. The anisotropy constant, K, is calculated as: 2.90 × 10^4 erg cm^{-3} for 300 K, 8.60 ×10^4 erg cm^{-3} for 5 K for system 1; 6.10 × 10^4 erg cm^{-3} for 300 K, 13.30 × 10^4 erg cm^{-3} for 5 K for system 2. Further, saturation magnetization, M_s, is calculated as 19.10 emu/g for system 1 at 300 K and 32.0 emu/g for 5 K for system 1, 32.80 emu/g and 66.0 emu/g at temperature 300 K and 5 K for system 2. An enhanced magneto-crystalline anisotropy is found in system 1 over system 2, in which high Zn substitution results enhanced anisotropic landscape.

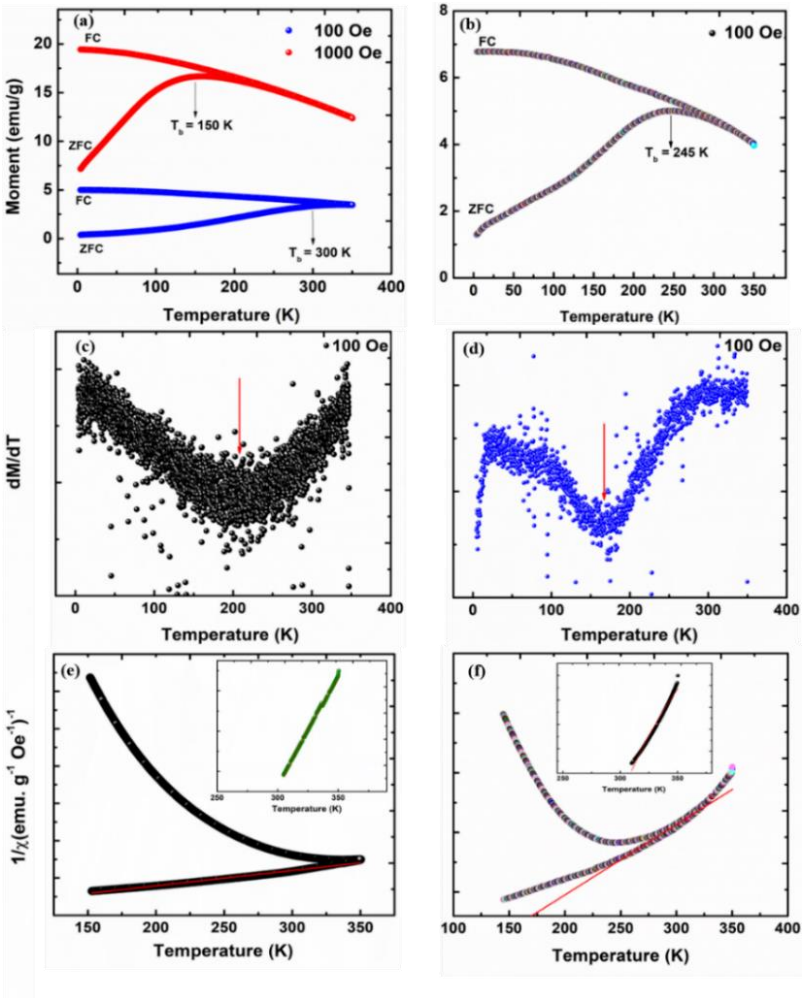

Figure 5.8: Temperature relying magnetization for (a) system 1, (b) system 2; dM/dT plot for (c) system 1, (d) system 2, Curie-Weiss (CW) fitting of (e) system

1, inset gives Griffiths Phase Fitting), (f) system 2 (inset gives Griffiths Phase Fitting). The blocking temperature is denoted in Figure (a, b).

To attain magnetic anisotropy details field dependent magnetization is analysed with the aid of random anisotropy theory (RAT) [53, 54, 55] as depicted in Figure 5.7(i). At 5 K, for 100 ≤ M ≤ 22500 Oe, equation 3.5 of Chapter 3, is used for fitting as depicted in Figure 5.7 (i). The anisotropy field H_r, exchange field H_{ex}, and saturation magnetization, M_0 are calculated at 5 K as 18991 Oe, 4463 Oe, 34.2 Oe for system 1; 14827 kOe, 3568 Oe, and 64 Oe for system 2. A decrease in the exchange field with Zn enhancement is found. Moreover, the strength of the random magnetic anisotropy field is decreasing with Zn substitution enhancement. An increment in saturation magnetization with octahedral site substitution is following a familiar trend as LAS model fitting. The strength of exchange field is high in system 1 compared to system 2 at low temperature.

The collective magnetic nature is further investigated by following temperature relying dc-magnetization for 2-350 K as given in Figure 5.8 at 100 Oe in ZFC and FC protocols. ZFC and FC profile shows bifurcation near 300 K and a relatively broad peak is evident because of the blocking state at 300 K, at 100 Oe. The SPM state is the reason for such blocking of spins. In order to further elucidate the SPM state transition, the ZFC/FC profile is calculated at 1000 Oe. With enhanced applied field, susceptibility is found to be increased and ZFC magnetization profile depicts a plateau. With enhancement in magnetic field, difference of ZFC and FC susceptibility ($\Delta\chi$) is found to be increased. The blocking temperature shifting is observed to 150 K. For system 2, ZFC-FC bifurcation is evident at 300 K, but blocking peak is observed at 245 K. Further, temperature-dependent dM/dT curve is considered to see the bifurcation as represented in Figure 5.8(b, e) [56]. The observed prominent dip at 200 K for system 1 and 170 K for system 2 confirms transition temperature. A modified Curie-Weiss (CW) law is considered similar to equation 3.6 of Chapter 3, as depicted in Figure 5.8(c, f). After fitting, the curie temperature, θ_{CW} ~200K is achieved for system 1 and 170 K for system

2. The Griffiths Phase (GP) fitting is executed for the temperature range above the blocking temperature [55, 56]. An expression is considered for power law of Griffith singularity as: $\chi^{-1} \propto (T - T_C^R)^{1-\lambda}$. Herein, λ is susceptibility exponent and T_C^R gives the temperature related to randomly oriented ferromagnetic clusters. χ^{-1} fitting is executed at high temperature as displayed in Figure 5.8(c, f) inset. The respective fitted values of λ are obtained in system 1 as 0.770 and 0.750 for system 2 at 100 Oe with a singularity. As λ lies in the range of 0 to 1, Griffiths phase existence is confirmed. The T_C^R is taken as similar to θ_{CW} during the calculation of λ. The fitted parameters ensure the possible presence of Griffiths phase-like nature above 300 K.

For a more detailed spin dynamic study, an ac susceptibility study is performed at 77 Hz, 317 Hz, 717 Hz, 1111 Hz, 3717 Hz, 6717 Hz, and 9717 Hz. A 10 Oe ac field is imposed without dc field and the respective temperature relying ac susceptibility is depicted in Figure 5.9((a), (b), (e), (f)) for real and imaginary components. The susceptibility follows an increasing trend with temperature and no temperature anomaly peak is observed till 350 K for system 1 in in-phase and out-of-phase components. As system 1 has room temperature blocking with higher exchange field, the spin-freezing nature may attain a temperature of more than 350 K [9]. However, a 1000 Oe dc field is superimposed with a 10 Oe ac field for frequencies: 3717 Hz, 6717 Hz, and 9717 Hz as depicted in Figure 5.9(c, d) [9]. A peak is seen at 150 K for all frequencies and there is no shift in temperature maxima peak. The achieved peak is the possible phase transition temperature, which is found to correlate with dM/dT plots. However, two peaks are seen in out-of-phase component at 16 K and 184 K. Additionally, a similar behaviour is seen for system 2 with a temperature maxima peak at 325 K as depicted in Figure 5.9(e). The component of out-of-phase gives a significant peak at 275 K for all frequency conditions. Indeed, easy axis orientation is investigated at 10 K following the FC magnetization trend. If system 2 is considered a system with randomly oriented easy axes, easy axes orientation can be evaluated with

equation 2.17 of Chapter 2. $\frac{M_{FC}^{align}}{M_{FC}}$ is found as 0.7, further confirming the possible existence of easy axis alignment in system 2.

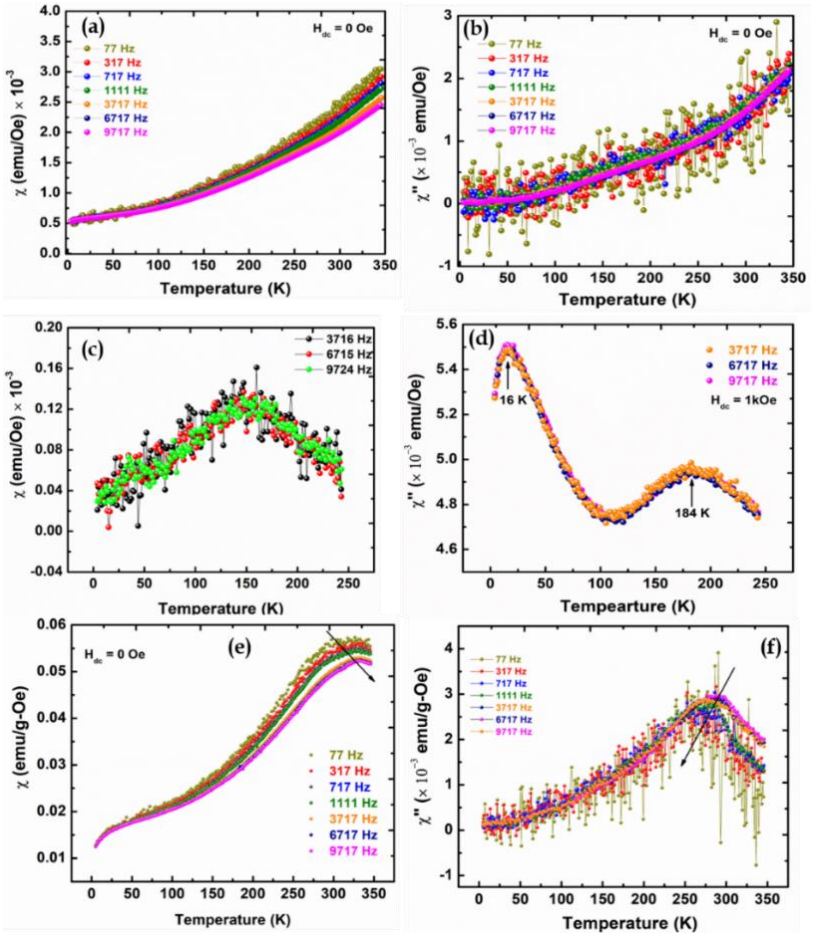

Figure 5.9: (a) Real component of ac susceptibility for system 1, (b) Imaginary ac susceptibility of system 2, (c) Real component of ac susceptibility with 1000 Oe dc field for system 1, (d) Imaginary component of ac susceptibility with 1000 Oe field for system 1, (e) Real component ac susceptibility for system 1, (f) Imaginary component ac susceptibility for system 2. The arrow mark indicates the change in the peak of T_{max} and χ_{max} with an increase in frequency. The freezing temperature is denoted in Figure (d).

5.4.4 Magnetic Resonance (MR)-relaxivity analysis

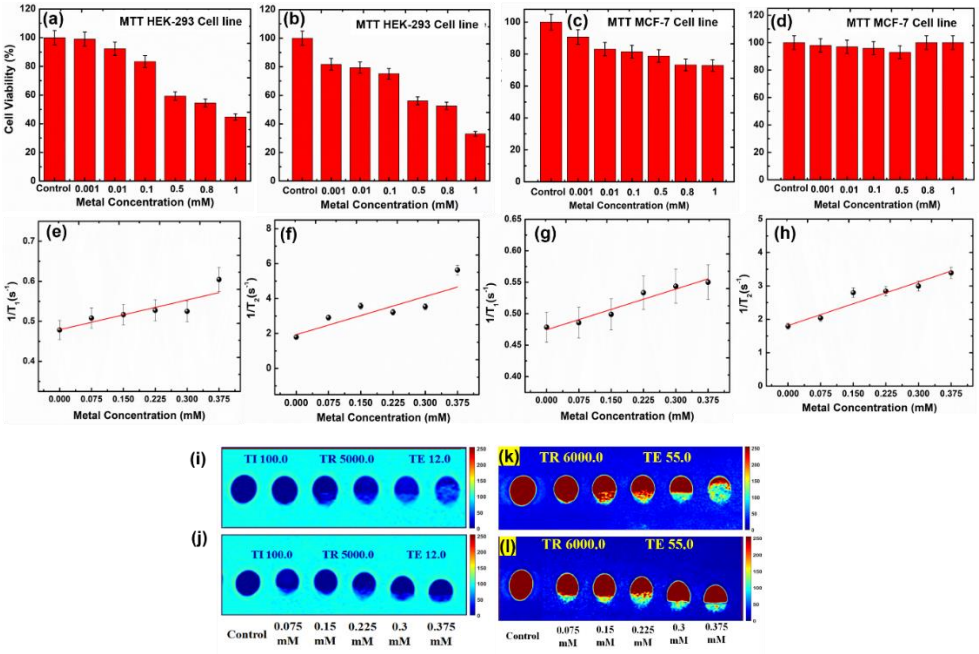

Figure 5.10: MTT assay at HEK cell-line for (a) system 1, and (b) system 2; MTT assay of MCF-7 cell in (c) system 1 and (d) system 2, Inverse longitudinal relaxation plot with metal concentration variation for (e) system 1 and (f) system 2; Inverse longitudinal relaxation time curve with metal concentration variation for (g) system 1 and (h) system 2; Phantom images of longitudinal (i) system 1, (j) system 2; Phantom images at various TE for (k) system 1, and (l) system 2. The error bars in the data present standard deviation in experimental data.

In vitro MTT assay is executed before the MR-relaxivity study, in order to get a detailed cytotoxicity analysis by considering a HEK293 cell line. The cell viability % exhibits good viability till 0.5 mM metal for both the systems as depicted in Figure 5.10(a) and Figure 5.10(b). Additionally, *in vitro* anticancer activity is performed by following the MTT assay for MCF-7 breast cancer cell-line and no pro-tumorigenic activity is evident for both systems as given in Figure 5.10(c, d). Therefore, MR-relaxivity analysis is done up to 0.375 mM metal concentration. However, the brightfield microscopic images are given in Appendix Section Figures A1 and A2.

In order to execute the MR-relaxivity study, five various metal concentrations are considered: 0.0750 mM, 0.150 mM, 0.2250 mM, 0.30 mmol, and 0.3750 mM for both systems as depicted in Figure 5.10(e-h). The achieved signal intensity is fitted for various inversion times (TI) at individual metal concentrations as [15, 12]:

$$M_{TI} = M_0[1 - 2\exp\frac{-TI}{T_1}] \quad (5.8)$$

M_{TI} in equation 5.8 is the respective signal intensity for each TI. TI is considered for 100-1500 ms for repetition time (TR) of 5000 ms with 12 ms, echo time (TE). The values for M_0 and T_1 are achieved after fitting. T_1 for individual metal concentrations are obtained and the fitting of $1/T_1$ with each metal concentration is depicted in Figure 5.10(e, g). The respective slope from the linear fitting gives a longitudinal relaxation rate, r_1. For fitting, follows expression is followed [15, 12]:

$$1/T_i = \frac{1}{T_{i(0)}} + r_i\, C \quad (5.9)$$

Here, Ti is the relaxation period in which i gives 1 for longitudinal relaxation and 2 for transverse relaxation. Ti(0) is the diamagnetic contribution of spin relaxation, and r_i gives relaxivity with respective metal concentrations, C. The respective spin-lattice relaxation time, r_1, is found as 0.240 $s^{-1}mM^{-1}$ and 0.220 $s^{-1}mM^{-1}$ for system 1 and system 2. The non-zero diamagnetic contribution for spin-orbit relaxation is achieved in the systems. However, transverse MR-relaxivity is explored following a similar protocol as per longitudinal relaxation with TE variation as, 10 ms to 180 ms for 6000 ms TR. The signal intensity for various TE can be fitted using the expression [15, 12]:

$$M_{TE} = M_0 exp\frac{-TE}{T_2} \quad (5.10)$$

Herein, M_{TE} is the signal intensity for individual TE. The fitted M_0 and T_2 values are achieved after executing a non-linear curve fitting curve considering each

metal concentration. T_2 for each metal concentration is considered to fit the following $1/T_2$ versus metal concentration curve as depicted in Figure 5.10 (f) and Figure 5.10 (h). The slope results transverse relaxation rate, r_2. r_2 is found as 7.30 $s^{-1}mM^{-1}$ and 4.30 $s^{-1}mM^{-1}$ for system 1 and system 2 for 3 T. However, the phantom image with metal concentration variation is depicted in Figure 5.10 (i, j) and Figure 5.10 (k, l) for longitudinal and transverse MR-relaxivity. With enhanced metal concentration, an improved phantom image signal is achieved with varied TI and TE. The dominance of spin-relaxation is confirmed from $\frac{r_2}{r_1}$ value. If $\frac{r_2}{r_1}$ results in a higher value than 10, and dominance of transverse relaxation is expected [8, 15, 12]. In the current scenario, $\frac{r_2}{r_1}$ is found as 30.0 for system1 and 19.50 for system 2. The dominance of MR-transverse relaxation is reflected in both systems.

According to the relation of the diffusive period of water protons, $\tau_{diff} = \frac{R^2}{C_{diff}}$, transverse relaxivity can be monitored by size variation in MNPs [58, 59, 60, 16, 17]. Herein R gives the radius of MNPs and C_{diff} is the water proton translation diffusivity. In the considered system, the radius of MNPs in their assembly arrangement is nearly equal. As a result, the diffusion period experienced by

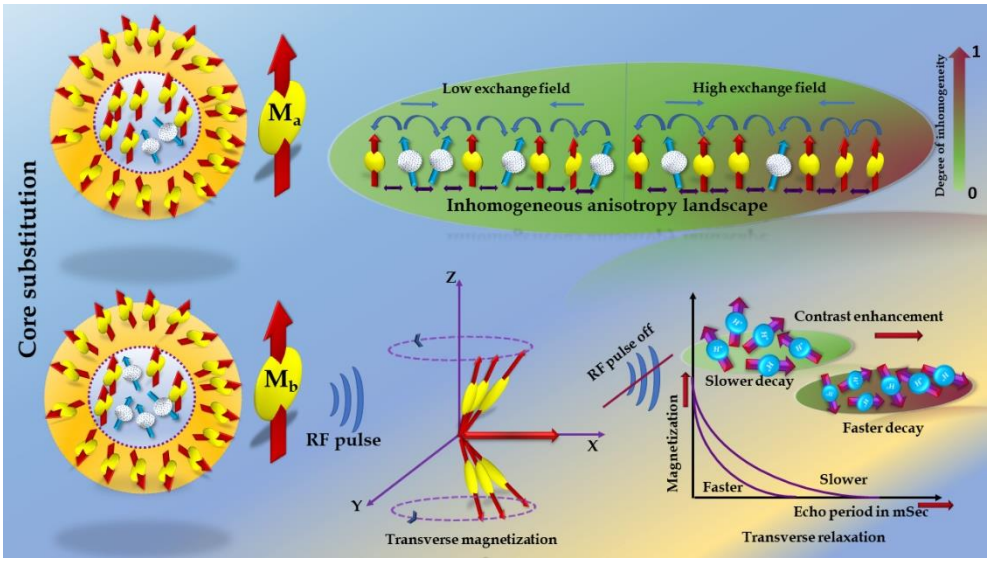

Figure 5.11: Schematic for enhancement in transverse relaxivity with variation in exchange field and inhomogeneous anisotropy landscape.

water protons will be the same for both cases. However, a variation in Larmor frequency can be experienced following the condition: $\Delta\omega = \frac{M_s \gamma_0 \mu_0}{3}$. Herein, γ_0 gives 2.67 × 10 8 rad $s^{-1}.T^{-1}$proton gyromagnetic ratio, and μ_0 is $4\pi \cdot 10^{-7}$ T ·m ·A^{-1}, vacuum magnetic permeability. As usual, M_s gives saturation magnetization. As r_2 is dependent on both $\Delta\omega$ and τ_{diff} in the region of MAR, the respective volume fraction γ can be addressed as $r_2 = (16/45)\ \gamma\tau_{diff}\ (\Delta\omega)^2$. In MAR condition [24, 25], $\Delta\omega\tau_{diff} < 1$, addresses a quick water molecules movement in relaxation. SDR condition [32] has been proven to be valid when a system exceeds the MAR threshold limitation. SDR works well for the condition, $\Delta\omega\tau_{diff} > 1$, and r_2 can be represented as: $(2\pi/9)\ \{\gamma\gamma_0(\mu_0 M_s)\}$. In both MAR and SDR regimes, r_2 is dependent on saturation magnetization and an enhancement in r_2 is achieved with enhanced saturation magnetization. However, in this case, $Ni_{0.75}Zn_{0.25}Fe_2O_4$@CoO with M_s of 19 emu/g demonstrates higher MR-transverse relaxivity than $Ni_{0.50}Zn_{0.50}Fe_2O_4$@CoO with M_s of 32.8 emu/g. In the case of complex assemblies, faster relaxation of water proton is not only because of saturation magnetization, but alignment in easy axes with anisotropy energy landscape are important factors. Furthermore, it is seen that the exchange field of the system can monitor the anisotropy landscape. This aforementioned insight is provided in Figure 5.11 of schematic representation. The system exhibits improved r_2 with greater MR-transverse relaxivity when it has a stronger exchange field strength, more asymmetricity in coercivity, aligned easy axes, lower magneto-crystalline anisotropy with lower saturation magnetization. Instead of taking into account the Larmor frequency change to create understanding in conflicting results, consideration of inherent parameters dependency provides a clearer understanding of transverse relaxation enhancement. The enhanced anisotropy landscape inhomogeneity offers an approach to get faster water protons relaxation.

5.5 CONCLUDING REMARKS

In this chapter, inhomogeneous anisotropy-dependent transverse MR-relaxivity enhancement is achieved by considering ensembles of isotropic nanoparticles of $Ni_{1-x}Zn_xFe_2O_4$@CoO (x=0.25, 0.50). Manipulation in inherent magnetic behaviour is employed herein by varying octahedral site substitution and MR-transverse relaxivity is explored. With change in magnetic linkage, the anisotropy field distribution is evident following 30 Oe asymmetric coercive field as well as 867 Oe exchange field, which makes the system $Ni_{0.75}Zn_{0.25}Fe_2O_4$@CoO a complex domain of anisotropy landscape. This triggers modulation in transverse relaxivity in $Ni_{0.75}Zn_{0.25}Fe_2O_4$@CoO as compared to $Ni_{0.5}Zn_{0.5}Fe_2O_4$@CoO. The simulation based on *ab initio* principle is utilised to investigate asymmetry behaviour of charge. In $Ni_{0.75}Zn_{0.25}Fe_2O_4$@CoO, the coercive field asymmetry triggers inhomogeneous anisotropy field having higher exchange coupling. Hence, besides magnetic susceptibility, exchange field-induced complex anisotropy can tune MR-transverse relaxivity. The unique results can be applied to clarify why intricate ensemble systems are inadequate for interpreting transverse effects in highly effective MRI applications.

References:

[1] Yang, L., Wang, Z., Ma, L., Li, A. Xin, J., Wei, R., Lin, H., Wang, R., Chen, Z. and Gao, J. The Roles of Morphology on the Relaxation Rates of Magnetic Nanoparticles. *ACS Nano,* 12:4605, 2018.

[2] Zhou, Z., Zhao, Z., Zhang, H., Wang, Z., Chen, X., Wang, R., Chen, Z. and Gao, J. Interplay between Longitudinal and Transverse Contrasts in Fe_3O_4 Nanoplates with (111) Exposed Surfaces. *ACS Nano,* 8:7976, 2014.

[3] Abdullah, A., Al-Wahaibi, Y., Bijeljic, B. and Muggeridge, A. Investigation of longitudinal and transverse dispersion in stable displacements with a high

viscosity and density contrast between the fluids. *Journal of Contaminant Hydrology,* 120:7976, 2011.

[4] Zhou, Z., Bai, R., Munasinghe, J., Shen, Z., Nie, L. and Chen, X. T_1–T_2 Dual-Modal Magnetic Resonance Imaging: From Molecular Basis to Contrast Agents. *ACS Nano*, 11:5227, 2017.

[5] Suárez-García, S., Arias-Ramos, N., Frias, C., Candiota, A. P., Arús, C., Lorenzo, J., Ruiz-Molina, D. and Novio, F. Dual T_1/T_2 Nanoscale Coordination Polymers as Novel Contrast Agents for MRI: A Preclinical Study for Brain Tumor. *ACS Applied Materials & Interfaces,* 10:38819, 2018.

[6] Matos, R., Gheata, A., Campargue, G., Vuilleumier, J., Nicolle, L., Pierzchala, K., Jelescu, I., Lucarini, F., Gautschi, I., Riporto, F., Dantec, R., Mugnier, Y., Chauvin, A., Mazzanti, M., Staedler, D., Diviani, D., Bonacina, L. and Gerber-Lemaire, S. Gd^{3+}-Functionalized Lithium Niobate Nanoparticles for Dual Multiphoton and Magnetic Resonance Bioimaging. *ACS Applied Nano Materials,* 5:2912, 2022.

[7] Mauri, M., Collico, V., Morelli, L., Das, P., Garcia, I., Avila, P., Bellini, M., Rotem, R., Truffi, M., Corsi, F., Simonutti, R., Liz-Marzan, L., Colombo, M. and Prosperi, D. MnO Nanoparticles Embedded in Functional Polymers as T_1 Contrast Agents for Magnetic Resonance Imaging. *ACS Applied Nano Materials,* 3:3787, 2020.

[8] Saikia, K., Bhattacharya, K., Sen, D., Kaushik, S. D., Biswas, J., Lodha, S., Gogoi, B., Buragohain, A. K., Kockenberger, W. and Deb, P. Solvent evaporation driven entrapment of magnetic nanoparticles in mesoporous frame for designing a highly efficient MRI contrast probe. *Applied Surface Science,* 464:567, 2019.

[9] Saikia, K., Sarma, D. D. and Deb, P. Organization dependent collective magnetic properties of secondary nanostructures with differential spatial

ordering and magnetic easy axis orientation. *Journal of Magnetism and Magnetic Materials,* 127:2016408, 2016.

[13] Scialla, S., Genicio, N., Brito, B., Florek-Wojciechowska, M., Stasiuk, G., Kruk, D., Bañobre-López, M. and Gallo, J. Insights into the Effect of Magnetic Confinement on the Performance of Magnetic Nanocomposites in Magnetic Hyperthermia and Magnetic Resonance Imaging. *ACS Applied Nano Materials,* 5:16462, 2022.

[15] Guleria, A., Pranjali, P., Meher, M. K., Chaturvedi, A., Chakraborti, S., Raj, R., Poluri, K. and Kumar, D. Effect of Polyol Chain Length on Proton Relaxivity of Gadolinium Oxide Nanoparticles for Enhanced Magnetic Resonance Imaging Contrast. *The Journal of Physical Chemistry C,* 123:18061, 2019.

[16] Solomon, I. Relaxation Processes in a System of Two Spins. *Physical Review,* 99:559, 1955.

[17] Bloembergen, N. and Morgan, L. Proton Relaxation Times in Paramagnetic Solutions. Effects of Electron Spin Relaxation. *The Journal of Chemical Physics,* 34:842, 1961.

[18] Lauffer, R. Paramagnetic metal complexes as water proton relaxation agents for NMR imaging: theory and design. *Chemical Reviews,* 87:901, 1987.

[19] Koenig, S. and Kellar, K. Theory of $1/T_1$ and $1/T_2$ NMRD profiles of solutions of magnetic nanoparticles. *Magnetic Resonance in Medicine,* 34:227, 1995.

[20] Bloembergen, N., Purcell, E. and Pound, R. Relaxation Effects in Nuclear Magnetic Resonance Absorption. *Physical Review,* 73:679, 1948.

[21] Gillis, P. and Koenig, S. Transverse relaxation of solvent protons induced by magnetized spheres: Application to ferritin, erythrocytes, and magnetite. *Magnetic Resonance in Medicine,* 5:323, 1987.

[22] Tong, S., Hou, S., Zheng, Z., Zhou, J. and Bao, G.; Coating Optimization of Superparamagnetic Iron Oxide Nanoparticles for High T_2 Relaxivity, *Nano Letters,* 10:4607–4613, 2010.

[23] Benetis, N., Kowalewski, J., Nordenskiold, L., Wennerstrom, H. and Westlund, P. Nuclear spin relaxation in paramagnetic systems: The slow motion problem for electron spin relaxation. *Molecular Physics,* 48:329, 1983.

[24] Freed, J. Dynamic effects of pair correlation functions on spin relaxation by translational diffusion in liquids. II. Finite jumps and independent T_1 processes. *The Journal of Chemical Physics,* 68:4034, 1978.

[25] Hwang, L. and Freed, J. Dynamic effects of pair correlation functions on spin relaxation by translational diffusion in liquids. *The Journal of Chemical Physics,* 63: 4017–4025, 1975.

[26] Tromsdorf, U., Bigall, N., Kaul, M., Bruns, O., Nikolic, M., Mollwitz, B., Sperling, R., Reimer, R., Hohenberg, H., Parak, W., Förster, S., Beisiegel, U., Adam, G. and Weller, H. Size and surface effects on the MRI relaxivity of manganese ferrite nanoparticle contrast agents. *Nano Letters,* 7:2422–2427, 2007.

[27] Jun, Y., Huh, Y., Choi, J., Lee, J. Song, H., Kim, S., Yoon, S., Kim, K., Shin, J., Suh, J. and Cheon, J. Nanoscale size effect of magnetic nanocrystals and their utilization for cancer diagnosis via magnetic resonance imaging. *Journal of the American Chemical Society,* 127:5732–5733, 2005.

[28] Zhao, Z., Zhou, Z., Bao, J., Wang, Z., Hu, J., Chi, X., Ni, K., Wang, R., Chen, X., Chen, Z. and Gao, J. Octapod iron oxide nanoparticles as high-performance T_2 contrast agents for magnetic resonance imaging. *Nature Communications,* 4:2266, 2013.

[29] Lee, N., Choi, Y., Lee, Y., Park, M., Moon, W., Choi, S. and Hyeon, T. Water-Dispersible Ferrimagnetic Iron Oxide Nanocubes with Extremely High r_2

Relaxivity for Highly Sensitive in Vivo MRI of Tumors. *Nano Letters,* 12:3127–3131, 2012.

[30] Sharma, V., Alipour, A., Soran-Erdem, Z., Aykut, Z. and Demir, H. Highly monodisperse low-magnetization magnetite nanocubes as simultaneous T_1–T_2 MRI contrast agents. *Nanoscale,* 7:10519, 2015.

[31] Voros, E., Cho, M., Ramirez, M., Palange, A., Rosa, E., Key, J., Garami, Z., Lumsden, A. and Decuzzi, P. TPA Immobilization on Iron Oxide Nanocubes and Localized Magnetic Hyperthermia Accelerate Blood Clot Lysis. *Advanced Functional Materials*, 25:1709, 2015.

[32] Bowen, C., Zhang, X., Saab, G., Gareau, P. and Rutt, B. Application of the static dephasing regime theory to superparamagnetic iron-oxide loaded cells. *Magnetic Resonance in Medicine,* 48:52–61, 2002.

[33] Gillis, P., Moiny, F. & Brooks, R. A. On T2-shortening by strongly magnetized spheres: A partial refocusing model. *Magnetic Resonance in Medicine,* 47, 257–263, 2002.

[34] Brooks, R., Moiny, R. and Gillis, P. On T_2-shortening by weakly magnetized particles: The chemical exchange model. *Magnetic Resonance in Medicine,* 45:1014–1020, 2001.

[35] Carroll, M., Woodward, R., House, M., Teoh, W., Amal, R., Hanley, T. and Pierre, T. Experimental validation of proton transverse relaxivity models for superparamagnetic nanoparticle MRI contrast agents. *Nanotechnology,* 21:035103, 2010.

[36] Zhou, Z., Tian, R., Wang, Z., Yang, Z., Liu, Y., Liu, G., Wang, R., Gao, J., Song, J., Nie, L. and Chen, X. Artificial local magnetic field inhomogeneity enhances T2 relaxivity. *Nature Communications,* 8:15468, 2017.

[37] Pothayee, N., Balasubramaniam, S., Pothayee, N., Jain, N., Hu, N., Lin, Y., Davis, R., Sriranganathan, N., Koretskyc, A. and Riffle, R. Magnetic nanoclusters with hydrophilic spacing for dual drug delivery and sensitive magnetic resonance imaging. *Journal of Materials Chemistry B,* 1:1142–1149, 2013.

[38] Balasubramaniam, S., Kayandan, Y., Lin, D., Kell, M., House, R., Woodward, T., Pierre, G., Riffle, J. and Davis, R. Toward Design of Magnetic Nanoparticle Clusters Stabilized by Biocompatible Diblock Copolymers for T_2-Weighted MRI Contrast. *Langmuir,* 30:1580–1587, 2014.

[39] Mohan, R., Ghosh, M. and Mukherjee, S. Large exchange bias effect in $NiFe_2O_4$/CoO nanocomposites. *Materials Research Express,* 5:035029, 2018.

[40] Wangchhuk, J. and Meher, S. Structural, electronic and magnetic properties of inverse spinel $NiFe_2O_4$: DFT+ U investigation. *Physics Letters A,* 443:128202, 2022.

[41] Idrissi, L.; Tahiri, N.; Omar, E.; Ez-Zahraouy, H.; J. Supercond. Nov. Magn. 2020, 33 1369-1375.

[42] Baldan, A. Review Progress in Ostwald ripening theories and their applications to nickel-base superalloys Part I: Ostwald ripening theories. *Journal of Materials Science,* 37:2171-2202, 2002.

[43] Pawar, C., Gujar, M. and Mathe, V. Optical Properties of Spin-Deposited Nanocrystalline Ni-Zn Ferrite Thin Films Processed by Sol-Gel. *Journal of Superconductivity and Novel Magnetism,* 30:615–625, 2017.

[44] Chen, Z. and Li, H. A novel phosphatizing strategy to engineering CoO/$Co_{1.94}$P@carbon polyhedron heterostructures for enhanced lithium-ion battery. *Journal of Materials Science,* 56:3346-3353, 2021.

[45] Mingqing, H., Le, X., Fen, C., Jiabiao, L., Yunpeng, H., Jian, B., Jingxia, Q., Yuanguo, X., Hui, X., Yan, Z. and Huaming, L. Hexamethylenetetramine-assisted

hydrothermal synthesis of octahedral nickel ferrite oxide nanocrystallines with excellent supercapacitive performance. *Journal of Materials Science,* 53:7621-7636, 2018.

[46] Bhosale, S., Ekambe, P., Bhoraskar, S. and Mathe, V. Effect of surface properties of $NiFe_2O_4$ nanoparticles synthesized by dc thermal plasma route on antimicrobial activity. *Applied Surface Science,* 441:724-733, 2018.

[47] Xu, D., Fan, D. and Shen, W. Catalyst-free direct vapor-phase growth of $Zn_{1-x}Cu_xO$ micro-cross structures and their optical properties. *Nanoscale Research Letters,* 8(1):46, 2013.

[48] Chaker, A., Alty, H., Tian, P., Kotsovinos, A., Timco, G., Muryn, C, Lewis, S. and Winpenny, R. Induced Chemical Networking of Organometallic Tin in a Cyclic Framework for Sub-10 nm Patterning and Interconnect Application. *ACS Applied Nano Materials,* 4:406-413, 2021.

[49] Silva, P. and Corminboeuf, C. Simultaneous Visualization of Covalent and Noncovalent Interactions Using Regions of Density Overlap. *Journal of Chemical Theory and Computation,* 10:3745–3756, 2014.

[50] Bora, M., Behera, S., Samal, P. and Deb, P. Magnetic proximity induced valley-contrasting quantum anomalous Hall effect in a graphene-$CrBr_3$ van der Waals heterostructure. *Physical Review B,* 105:235422, 2022.

[51] Rana, R., Pandey, P., Singh, R. and Rana, D. Positive exchange-bias and giant vertical hysteretic shift in $La_{0.3}Sr_{0.7}FeO_3/SrRuO_3$ bilayers. *Scientific Reports,* 4:4138, 2014.

[52] Silva, F., Depeyrot, J., Raikher, Y., Stepanov, V., Poperechny, I., Aquino, R., Ballon, G., Geshev, J., Dubois, E. and Perzynski, R. Exchange-bias and magnetic anisotropy fields in core–shell ferrite nanoparticles. *Scientific Reports,* 11:5474, 2021.

[53] E. M. Chudnovsky, W. M. Saslow, and R. A. Serota, Ordering in ferromagnets with random anisotropy. *Physical Review B,* 33:251, 1986.

[54] Aharony, A. and Pytte, E. Infinite Susceptibility Phase in Random Uniaxial Anisotropy Magnets. *Physical Review Letters,* 45:1583, 1980.

[55] Yadav, K., Sharma, M., Singh, S. and Mukherjee, K. Exotic magnetic behaviour and evidence of cluster glass and Griffiths like phase in Heusler alloys $Fe_{2-x}Mn_xCrAl$ ($0 \leq x \leq 1$). *Scientific Reports,* 9:15888, 2019.

[56] Saha, S., Dutta, A., Gupta, S., Bandyopadhyay, S. and Das, I. Origin of the Griffiths phase and correlation with the magnetic phase transition in the nanocrystalline manganite $La0.4(Ca_{0.5}Sr_{0.5})_{0.6}MnO_3$. *Physical Review B,* 105: 214407, 2022.

[57] Ghanta, S., Das, A., Jana, P., Vrtnik, S., Gačnik, D., Luzar, J., Jelen, A., Koželj, P., Wencka, M. and Dolinšek, J. Structure and Spin-Glass Magnetism of the $Mn_xNi_2Zn_{11-x}$ Pseudobinary γ-Brasses at Low Mn Contents. *Inorganic Chemistry,* 60:12226, 2021.

[58] Haan, H. Mechanisms of proton spin dephasing in a system of magnetic particles. *Magnetic Resonance in Medicine,* 66:1748–1758, 2011.

[59] Vuong, Q., Berret, J., Fresnais, J., Gossuin, Y. and Sandre, O. A. Universal Scaling Law to Predict the Efficiency of Magnetic Nanoparticles as MRI T_2-Contrast Agents. *Advanced Healthcare Materials,* 1:502–512, 2012.

[60] Thapa, B., Diaz-Diestra, D., Badillo-Diaz, D., Sharma, R., Dasari, K., Kumari, S., Holcomb, M., Beltran-Huarac, J., Weiner, B. and Morell, G. Controlling the transverse proton relaxivity of magnetic graphene oxide. *Scientific Reports,* 9:5633, 2019.